 CMES, vol.3, no.3, pp.367-380, 2002

Computational Modeling of Shock and Impact Response of Alumina

A. M. Rajendran[1], **D. J. Grove**[2]

Abstract: This paper presents detailed computational analyses investigating the ability of constitutive relationships to describe the response of a 99.5% pure alumina (AD995) subjected to a wide range of stress/strain loading states. Using a shock-wave-propagation-based finite element code, one and two-dimensional simulations were performed for the following shock and impact configurations: plate-on-plate impact; rod-on-rod impact; single-density plate-on-rod impact; graded-density plate-on-rod impact; and rod penetration into a thick plate. The detailed analyses presented in this paper include a model constant sensitivity study through comparisons of computed wave profiles with experimental measurements.

keyword: microcracking, ceramic damage model, constitutive equations, shock, impact, alumina.

1 Introduction

Due to the advent of high performance computing capabilities in recent years, armor/anti-armor designers often rely on computational codes to evaluate the feasibility of novel concepts. One of the most important aspects of a computational mechanics approach involves implementation, verification, and validation of numerical algorithms to describe the mechanical response of materials. Since ceramic materials are often employed in vehicular and personnel armor systems, accurate constitutive relations are required to facilitate reliable computational and engineering analyses involving ceramic deformation and fracture. Recently, several constitutive damage models for ceramic materials [Rajendran and Kroupa (1989), Addessio and Johnson (1990), Steinberg (1991), Johnson and Holmquist (1994), Rajendran (1994) / Rajendran and Grove (1996), Espinosa (1995), and Simha (1998)] have been implemented in various finite element/difference codes. This paper addresses the issues involved in evaluating the generality of the present constitutive model's constants for 99.5% pure aluminum oxide (AD995) through computer simulations of a variety of shock and penetration experiments. Well-controlled impact techniques and high-resolution diagnostics are generally used to both calibrate and validate ceramic constitutive models. Validation of ceramic material models under multi-axial loading conditions requires reliable diagnostic measurements from shock and impact experiments wherein the ceramic targets experience three-dimensional stress/strain loading conditions.

This paper further investigates the ability of the present constitutive model to capture the various salient features of experimentally measured shock wave profiles. The following experimental configurations were simulated using the EPIC code (Johnson, Stryk, Holmquist, and Beissel (1997)): 1) low and high velocity plate impact experiments; 2) a short ceramic rod impacting a long ceramic rod; 3) an aluminum plate impacting a long slender AD995 ceramic rod; 4) a graded density flyer plate impacting a ceramic rod with and without a steel sleeve; and 5) a long tungsten rod penetrating a target consisting of a laterally confined AD995 ceramic tile backed by a thick steel block.

2 Constitutive Model for Ceramics

The ceramic model employed in this study (Rajendran (1994), Rajendran and Grove (1996)) assumes the following: 1) preexisting randomly distributed flaws, 2) plastic flow and pore collapse when shocked above the Hugoniot elastic limit (HEL), 3) no plastic flow in tension, 4) degradation of elastic moduli under both compression and tension due to microcracking, and 5) pulverization at a critical crack density. Due to low fracture toughness, microcracking occurs in the ceramic at relatively low tensile stress amplitudes. The model employs a strain-rate-dependent strength relationship to describe the response of the ceramic material due to inelastic (plastic) deformation under high-compression pressure. The deviatoric stresses are calculated using a con-

[1] ARO, ARL, RTP, NC, USA.
[2] ARL, APG, MD, USA.

ventional radial return approach that is often used in viscoplasticity models. The plastic strains are subtracted from the total strains to obtain the elastic strains. The elastic stress-strain relationship for the microcracked aggregate material is given by the following rate equation:

$$\dot{\sigma}_{ij} = M_{ijkl}\,(\,\dot{\varepsilon}_{kl} - \dot{\varepsilon}^{p}_{kl}\,) \tag{1}$$

where $\dot{\sigma}_{ij}$ is the total stress rate, $\dot{\varepsilon}_{kl}$ is the total strain rate, $\dot{\varepsilon}^{p}_{kl}$ is the plastic strain rate due to viscoplastic flow and pore collapse, the strain rate difference $(\dot{\varepsilon}_{kl} - \dot{\varepsilon}^{p}_{kl})$ is the elastic strain rate, and the components of the stiffness tensor M are given by Rajendran (1994). After damage initiates, the unloading and reloading paths follow the degraded elastic modulus (secant modulus), thus allowing full recovery of strains due to microcracking. The elements of the stiffness matrix are functions of the model's dimensionless microcrack density parameter γ, where $\gamma = N^{*}_{o}\,a^{3}$. N^{*}_{o} is the average number of microflaws per unit volume, and a, the maximum microcrack size, is treated as an internal state variable. The model assumes that pore collapse is due to local microscopic plastic flow in the matrix material surrounding the pores. The pore collapse strain components were derived from the pressure dependent yield surface of Gurson (1977). The compressive strength of the intact ceramic material is described by a strain rate dependent relationship:

$$Y = A\,(\;1\;+\;C\;\ln\dot{\varepsilon}\;) \tag{2}$$

where A is the quasi-static maximum strength, C is the strain rate sensitivity parameter, and $\dot{\varepsilon}$ is a normalized (dimensionless) equivalent plastic strain rate. It is possible to account for the development of anisotropy due to changes in the shape and orientation of the voids during deformation as recently suggested by Kailasam, Aravas, and Castañeda (2000).

The microcracks extend when the stress state satisfies a generalized criterion proposed by Margolin (1984). The microcrack extension causes the microcrack density γ to increase, which results in stress relaxation in the cracked ceramic material. Since N^{*}_{o} is assumed to be a constant, the increase in γ is entirely due to the increase in the crack size a. The damage evolution law is described by,

$$\dot{a} \;=\; n_1\,C_R\left[\,1\;-\;\left(\frac{G_{cr}}{G^{\pm}_{I}}\right)^{n_2}\,\right] \tag{3}$$

where C_R is the Rayleigh wave speed, G_{cr} is the critical strain energy release rate for microcracking, and $G^{\pm}_{I}$ are the applied strain energy release rates (G^{+}_{I} for mode I, and G^{-}_{I} for modes II/III). The parameters n_1 and n_2 (used to control the crack growth rate) are always assumed to be equal to 1.0, except for mode II/III crack extension, when n_1 is generally assumed to be equal to 0.1. G_{cr} is calculated from the fracture toughness K_{IC}, and the $G^{\pm}_{I}$ are calculated as,

$$G^{+}_{I} = \frac{4(1-\nu^2)\,a}{\pi E}\left[\sigma^{2}_{kk} + \frac{2(\sigma^{2}_{ik}+\sigma^{2}_{jk})}{(2-\nu)}\right],\; i\neq j\neq k \tag{4}$$

$$G^{-}_{I} = \frac{8(1-\nu^2)\,a}{\pi E(2-\nu)}\left[\sqrt{\sigma^{2}_{ik}+\sigma^{2}_{jk}} + \mu\sigma_{kk}\right]^{2},\; i\neq j\neq k \tag{5}$$

where E is Young's modulus, ν is Poisson's ratio, and μ is the dynamic friction coefficient. Microcrack opening occurs when G^{+}_{I} exceeds G_{cr}, or microcrack extension occurs when G^{-}_{I} exceeds G_{cr}.

To describe the pressure variation with respect to volumetric compressive strain, the following modified Mie-Gruneisen relationship for the equation of state (EOS) was employed:

$$P = K_{\gamma}(b_1\eta + b_2\eta^2 + b_3\eta^3)(1 - \;0.5\Gamma\eta\,) \tag{6}$$

where η is the elastic volumetric compressive strain, Γ is the Mie-Gruneisen parameter, b_1, b_2, and b_3 are empirical parameters used to fit the Hugoniot curve, and K_{γ} is the ratio of the degraded bulk modulus to the intact bulk modulus.

The ceramic model considers the material to be in a comminuted (pulverized) state when the crack density parameter γ exceeds a critical value (0.75) during compressive loading. Once pulverization has occurred, the compressive strength of the comminuted material (Y_p) is described by the Mohr-Columb law,

$$Y_p = \beta_p P \tag{7}$$

where P is the pressure, and the model parameter β_p represents the dynamic friction coefficient for granular motion. Another model parameter, $Y^{\max}_{p}$, was introduced to

impose an upper limit on the compressive strength of the pulverized ceramic material.

To describe the dynamic response of the AD995 ceramic, we employed a value of 3.89 g/cm ^{3} for the density, a value of 156 GPa for the shear modulus, and the following EOS parameters: Γ = 2.3, b_1 = 231 GPa, b_2 = -160 GPa, and b_3 = 2774 GPa. The calibrated constants for the present ceramic constitutive damage model were: A = 2.3 GPa, C = 0.2, $K_{IC} = 3MPa\sqrt{m}$, $a_o = 20\mu$m, $N_o^* = 2x10^{11}$ m^{-3}, n_1^-= 0.1 (for mode II crack extension), μ = 0.45, β_p= 1, and $Y_p^{\max}$= 4.5 GPa.

3 Modeling and Simulations

Determination of the dynamic response of ceramics often involves various types of shock and projectile penetration experiments. We considered the following five impact configurations: 1) *plate impact* $\sim$ a thin flyer plate impacting a thick target plate, 2) *rod-on-rod impact* $\sim$ a short slender ceramic rod impacting a long slender ceramic rod, 3) *single-density plate-on-rod impact* $\sim$ a thin flyer plate impacting a long ceramic rod, 4) *graded-density plate-on-rod impact* $\sim$ a graded-density flyer plate impacting a slender ceramic rod with and without a confining steel sleeve, and 5) *projectile penetration* $\sim$ a tungsten long rod penetrating a laterally confined ceramic tile backed by a steel block.

Numerical simulations can often be used to help interpret the diagnostic measurements from complex impact experiments. Most models are unable to accurately predict the fracture evolution in brittle materials due to the very complex crack nucleation and propagation processes. However, sensitivity studies of the model parameters often yield insights that can guide armor designers to develop advanced concepts.

To simulate the various experimental configurations, we used the 1999 version of the EPIC finite element code. EPIC is a well-established three-dimensional production code that was initially developed in the early 1970's to describe the response of solid materials to dynamic impact loading. Johnson, Stryk, Holmquist, and Beissel (1997) have described the details of this explicit Lagrangian finite element code. We implemented the present constitutive model in the 1999 version of EPIC. To maintain the stability of the explicit finite element solution, an iterative scheme (described by Cook, Rajendran, and Grove (1992)) based on a second-order diagonally implicit Runge-Kutta method was employed in the model solution algorithm.

In the EPIC simulations, we assumed no friction between the contacting surfaces. The code employs a traditional contact algorithm to adjust the positions and velocities of slave nodes and master surface nodes. Multiple iterations are required to achieve good velocity and position matches of the slave nodes with the master segments.

When simulating the plate impact experiments (see Section 3.1), EPIC's one-dimensional (1-D) uniaxial strain option was invoked; the element size (nodal spacing) used for these 1-D computations was 0.01 cm. The remaining test configurations were simulated using EPIC's two-dimensional (2-D) axisymmetric option. In these simulations, a cross-triangular element arrangement was employed, and the grid sensitivity of the model solution was evaluated by comparing the results from "regular" and "fine" finite element grids; the spacing between the primary nodes was 0.1 cm for the "regular" grids and 0.05 cm for the "fine" grids.

3.1 Plate Impact Simulations

In plate impact experiments, a flat thin disk (plate) is made to impact against a target plate. In the present study, experimental data for high-pure AD995 alumina from two different sources were considered: a low velocity experiment (flyer thickness: 4 mm, target thickness: 8 mm, impact velocity: 83 m/s) performed by Dandekar and Bartkowski (1994), and a high velocity experiment (flyer thickness: 5 mm, target thickness: 10 mm, impact velocity: 1943 m/s) reported by Grady and Moody (1996).

Dandekar and Bartkowski glued a PMMA window to the back of the ceramic target plate and used an embedded stress gauge to record the stress history at the target/window interface. Grady and Moody glued a lithium fluoride window to the back of the ceramic target plate and employed a velocity interferometry system (VISAR) to record the particle velocity history at the target/window interface. Using the EPIC code's 1-D strain option, simulations of these experiments were performed to calibrate the model constants. As previously mentioned, an element size (nodal spacing) of 0.01 cm was employed in the computations.

Figure 1 compares the model calibration with the experimental data for both the low and high velocity AD995

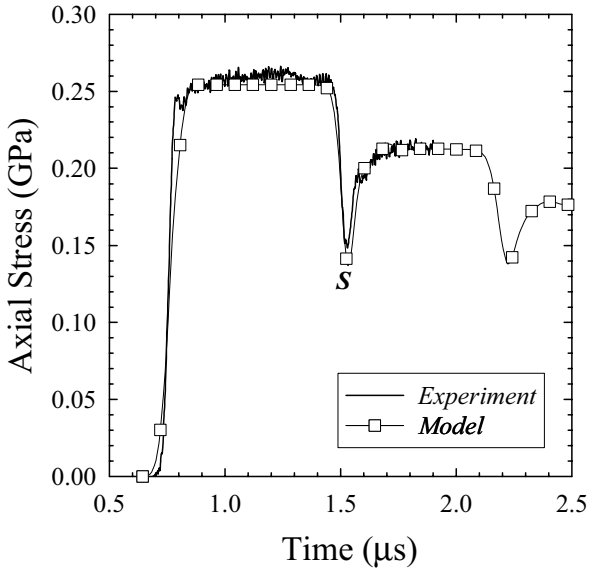

(a) Low velocity plate impact test

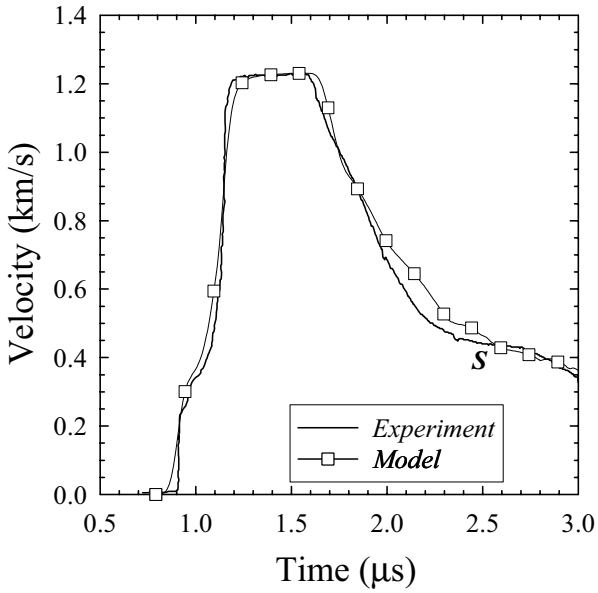

(b) High velocity plate impact test

Figure 1 : Comparison of computed axial stress and velocity histories with data from AD995 plate impact tests performed under one-dimensional strain conditions

plate impact tests. The spall signals (profiles beyond point ***S***) closely matched the data. A 20-μm initial crack size (a_o) was required to satisfy the Griffith criterion in order to match the arrival time of the spall signal in the low-velocity impact test (point ***S*** in Fig. 1). In the high-velocity impact test, the computed spall signal was relatively insensitive to the value of a_o (down to about 1 μm).

3.2 Rod-on-Rod Impact Simulations

Recently, Simha (1998) considered a short AD995 alumina rod impacting a long AD995 alumina rod. In this uniaxial stress configuration, shown schematically in Fig. 2(a), a short slender ceramic rod impacts a long ceramic rod having a length-to-diameter ratio (L/D) of about 8. A stress gauge is typically embedded in the target rod to record the stress history.

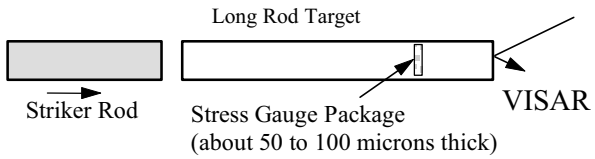

(a) Test configuration schematic

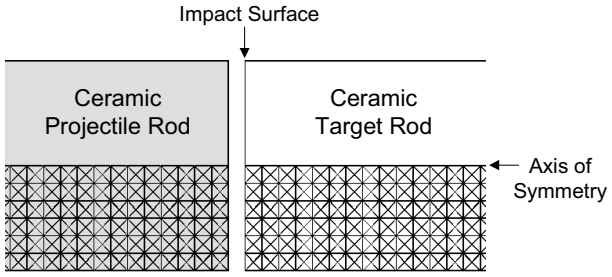

(b) Finite element grid (2D axisymmetric)

Figure 2 : Rod-on-rod impact (uniaxial stress state)

In these experiments, fracture initiates at the impact end, with several splitting type macrocracks forming and propagating toward the gauge location. The measured peak stress from this experiment can be used in a qualitative sense to validate the model constants under a uniaxial stress state. Attempting to model this macrocrack propagation using a continuum-mechanics-based finite element code will not be accurate; codes based on a meshless method such as that proposed by Kim and Atluri (2000) would be more suitable.

Using the 2D axisymmetric geometry option in EPIC, the rod-on-rod impact configuration described above was simulated for two different impact velocities (0.175 km/s and 0.278 km/s). The striker rod was 5 cm long and 1.25

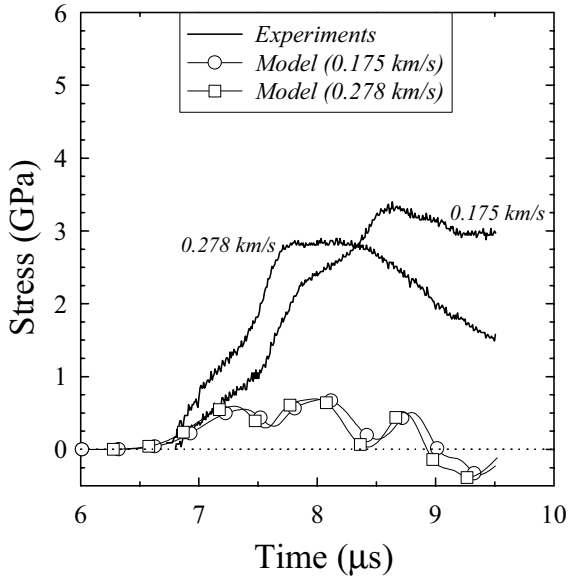

Figure 3 : Comparison of computed (a_o = 20 μm) stress histories with data from rod-on-rod impact tests

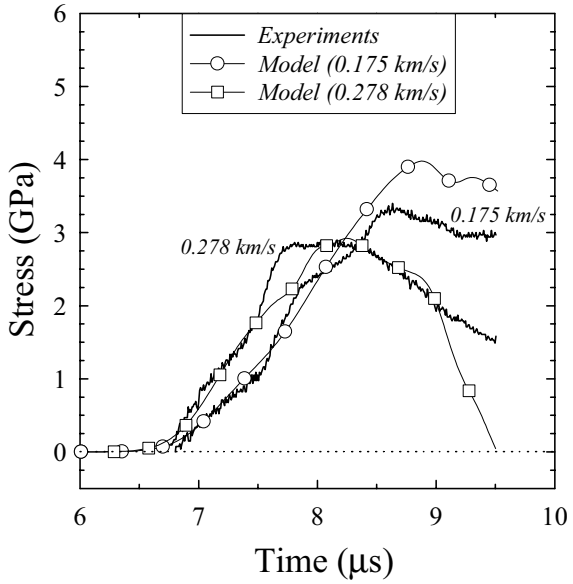

Figure 4 : Comparison of computed (a_o = 1.3 μm) stress histories with data from rod-on-rod impact tests

cm in diameter (L/D = 4), while the target rod was 10 cm long and 1.25 cm in diameter (L/D = 8). The baseline model constants for AD995 (see Section 2) were employed in the simulations.

In the "regular" finite element grid (0.1 cm spacing), 657 nodes and 1200 elements were used to describe the projectile rod, while 1307 nodes and 2400 elements were used to describe the target rod. Figure 2(b) depicts a portion of the "regular" grid in the vicinity of the impact region. The "fine" (0.05 cm spacing) grid required 2513 nodes / 4800 elements for the projectile rod, and 5013 nodes / 9600 elements for the target rod.

Figure 3 compares the model-predicted stress histories with the experimental data. The measured peak stress levels (3 - 3.5 GPa) are significantly higher than those predicted by the model ($<$ 1 GPa). In the model, crack damage initiates when the applied strain energy release rate exceeds a critical value, according to a generalized Griffith criterion. For a 20-μm initial crack size, the applied strain energy release rate exceeded the critical strain energy release rate, causing almost instantaneous fracture initiation upon impact. As a result, release waves from the impact end followed and overtook the initial shock front; this significantly reduced its amplitude.

To investigate the effects of delaying the onset of fracture, the rod-on-rod impact experiments were re-simulated with several smaller initial crack sizes. As Fig. 4 indicates, the model-generated peak stress levels (with a_o = 1.3 μm) now match the experimental values. However, for this 1.3-μm initial crack size, the Griffith criterion was not met in the case of low-velocity plate impact, so the model was unable to reproduce the measured spall signal (see Fig. 1(a)). The large initial crack size (20 μm) required to satisfy the Griffith criterion in the low velocity plate impact test simulation results in premature and excessive damage evolution in the rod-on-rod impact simulations.

Figure 5 further illustrates the effect of the initial flaw size on the model-predicted damage evolution. In this figure, cross-sectional damage contour plots from two simulations of the lower velocity (0.175 km/s) rod-on-rod impact test are compared at 1, 2, and 10 microseconds (μs); the darkest gray regions represent totally failed (comminuted) ceramic material, while the lighter shades of gray indicate lower levels of damage. The only difference between the simulations was the initial flaw size a_o (1.3 μm vs. 20 μm). As the figure indicates, the larger a_o results in rapid and extensive damage accumulation at the impact surfaces of both the projectile and target rods, while the smaller a_o delays the initiation of microcracking and significantly reduces the overall extent of the damaged regions.

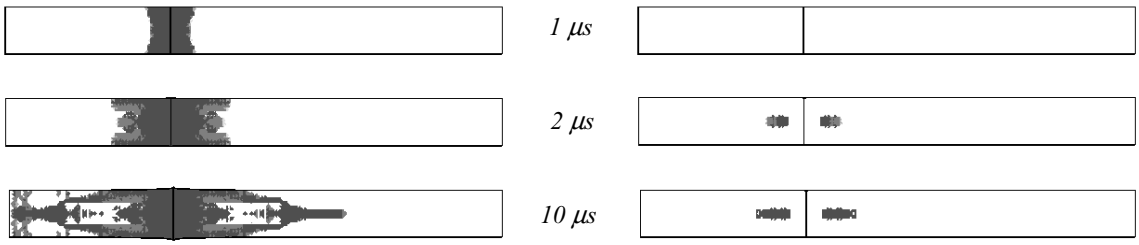

(a) a_o = 20 μm (b) a_o = 1.3 μm

Figure 5 : Effect of initial flaw size on model-predicted damage (shaded regions), from rod-on-rod impact simulations (impact velocity = 0.175 km/s)

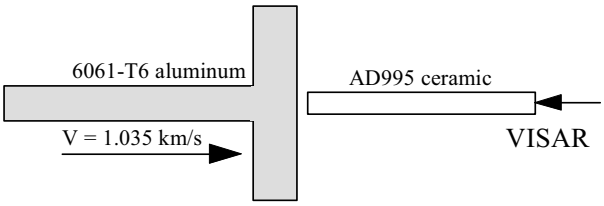

(a) Test configuration schematic

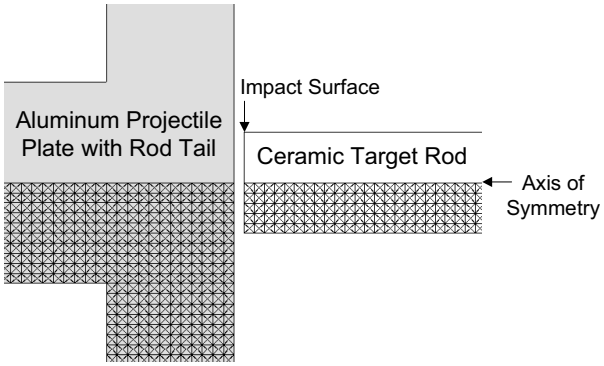

(b) Finite element grid (2D axisymmetric)

Figure 6 : Single-density plate-on-rod impact

The model solutions for the rod-on-rod impact simulations were relatively insensitive to the finite element grid. The velocity profiles from the "regular" and "fine" grids were very similar, with nearly identical peak velocity levels (for both impact velocities). The damaged regions were a little more extensive in the "fine"-grid calculations, but the damage patterns were the same as those predicted by the "regular" grids. Numerical results from continuum damage mechanics based constitutive relationships usually exhibit some degree of mesh sensitivity which can be minimized or eliminated using a damage diffusive equation as suggested by Chen, Hu, and Chen (2000).

3.3 Single-Density Plate-on-Rod Impact Simulations

Grady and Wise (1993) reported an impact configuration in which a flat 6061-T6 aluminum plate (diameter = 8.9 cm, thickness = 1.27 cm) with a long trailing rod (diameter = 2 cm, length = 12.2 cm) was made to impact a stationary long ceramic rod (diameter = 1 cm, length = 8 cm) at a velocity of 1.035 km/s.

The rod section of the flyer plate prevents strong release waves from entering the ceramic rod, thus keeping the ceramic under compression for a longer period of time. Shown in Fig. 6(a), this configuration permits a time-resolved investigation of the dynamic response of materials under a multi-axial strain state. The stress state in the ceramic rod well away from the impact face is uniaxial. During the experiment, time-resolved particle velocity data were obtained at the free end of the target rod.

Using the 2D axisymmetric option, we simulated the plate-on-rod impact configuration shown in Fig. 6. In the "regular" finite element grid (0.1 cm spacing), 3528 nodes and 6712 elements were used to describe the aluminum flyer plate (with attached rod), while 886 nodes and 1600 elements were used to describe the ceramic rod. Figure 6(b) depicts a portion of the "regular" grid in the vicinity of the impact region. The "fine" (0.05 cm spacing) grid required 13816 nodes / 26944 elements for the aluminum plate/rod, and 3371 nodes / 6400 elements for the ceramic rod.

Figure 7 compares the model-predicted (a_o = 20 μm) velocity history with the experimental data. We have also shown the elastic (no crack damage) solution in this figure. The measured peak velocity ($\approx$ 0.180 km/s) is sub-

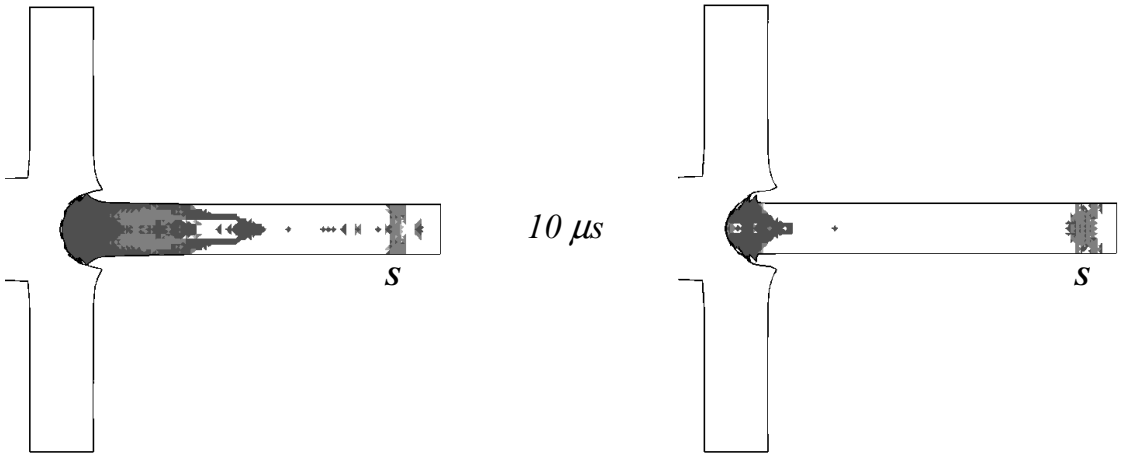

(a) a_o = 20 μm (b) a_o = 0.75 μm

Figure 8 : Effect of initial flaw size on model-predicted damage (shaded regions), from plate-on-rod impact simulations

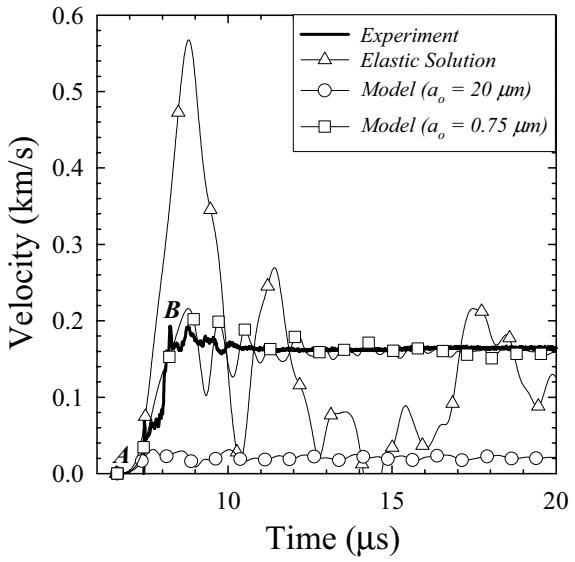

Figure 7 : Comparison of computed velocity histories (elastic, a_o = 20 μm, and a_o = 0.75 μm) with data from single-density plate-on-rod impact test

stantially lower than that of the elastic solution ($\approx$ 0.568 km/s) due to fracturing of the ceramic rod. The extremely low peak velocity level predicted by the model ($\approx$ 0.020 km/s) was caused by premature fracture resulting from the large initial crack size (20 μm). To investigate the effects of delaying the onset of damage in this configuration, the experiment was re-simulated using smaller values for the initial crack size.

As Fig. 7 indicates, the calculated velocity history (with a_o = 0.75 μm) shows reasonable agreement with the measured velocity profile. Since it is not possible to recover the ceramic rod after the experiments, the VISAR signal interpretation often requires additional detailed simulations of the experiment. In Fig. 7, the measured velocity reaches a peak at point ***B*** and then becomes fairly constant when the free end of the rod "spalls off". Our computational analysis revealed that the amount of reduction in the maximum velocity (as compared to the elastic solution) was about 0.400 km/s; this was due to elastic release waves from the damaged portion of the ceramic rod near the impact end. The release waves from the impact end of the rod continue to unload until spall occurs in the rod. With the larger initial flaw size (a_o = 20 μm), the model prematurely predicted the formation of a spall plane by 8.4 μs. This is the time at which the stresses at the spall location became tensile due to complex wave interactions. However, with a_o = 0.75 μm, the spall plane formation was delayed until about 9.1 μs, resulting in an excellent match with the measured peak velocity level. This 0.7-μs delay was sufficient to allow the particle velocity to reach the measured peak. Figure 8 shows the damage contours for the two simulations (20 μm and 0.75 μm) at 10 μs. The darkest regions (mode II microcracking) in the figure represent totally failed (comminuted) ceramic material, while the lighter shades of gray indicate lower levels of damage. The larger value of a_o (20 μm) results in more rapid and extensive damage accumulation at the impact surface of the ceramic rod, while the

smaller value (0.75 μm) delays the initiation of microcracking and significantly reduces the overall extent of the damaged regions. Both simulations predicted spallation near the free end of the rod (at location ***S*** in Fig. 8).

The model solution for the plate-on-rod impact simulation was fairly insensitive to the finite element grid. For a_o = 0.75 μm, the initial portion of the velocity history from the "fine"-grid calculation was nearly identical to that of the "regular" grid. Beyond 10 μs, the "fine"-grid velocity history exhibited significantly more "noise" (oscillations), with an average velocity level of around 0.150 km/s (about 6% lower than that of the "regular" grid). The predicted damage patterns were similar for both grids, with damage forming only at the impact end and near the free end (spall plane) of the ceramic rod.

3.4 Graded-Density Plate-on-Rod Impact Simulations

Recently, Chhabildas, Furnish, Reinhart, and Grady (1998) reported an experimental configuration in which an AD995 ceramic rod (L/D $\approx$ 4, sleeved or unsleeved) was impacted by a graded-density flyer plate consisting of extremely thin (0.1-cm thick) layers of titanium, aluminum, and TPX bonded to a 1.9-cm thick steel plate. A VISAR was used to record the axial particle velocity of the free end of the target rod. A schematic of this configuration is shown in Fig. 9(a).

To investigate the ability of the model constants to capture the salient features of the measured wave profiles, we used the 2D axisymmetric option in EPIC to simulate the graded-density plate-on-rod impact configuration for both bare and sleeved AD995 ceramic target rods. For diagnostic purposes, Chhabildas, Furnish, Reinhart, and Grady (1998) employed a VISAR to record the axial velocity history of the ceramic rod's free surface. The experimental impact velocities were 0.300 km/s for the bare-rod case, and 0.321 km/s for the sleeved-rod case.

The graded-density flyer plate was modeled as a circular disk with a diameter of 5 cm and a thickness of 2.2 cm, consisting of layers of steel (1.9 cm thick), titanium (0.1 cm thick), aluminum (0.1 cm thick), and TPX (0.1 cm thick). The lowest density material (TPX) was on the flyer plate's impact surface, and the density increased with each successive material layer: TPX (0.820 g/cm^3) $\rightarrow$ aluminum (2.704 g/cm^3) $\rightarrow$ titanium (4.424 g/cm^3) $\rightarrow$ steel (7.823 g/cm^3). A continuous finite element grid was employed in the flyer plate

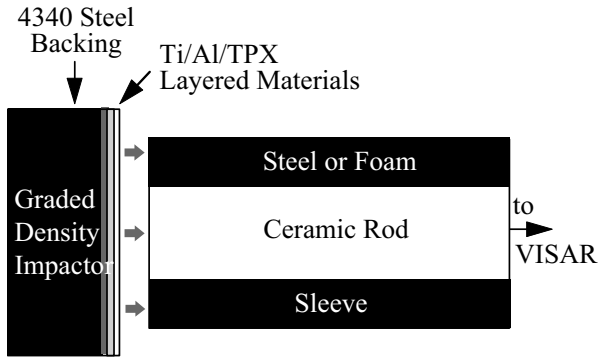

(a) Test configuration schematic

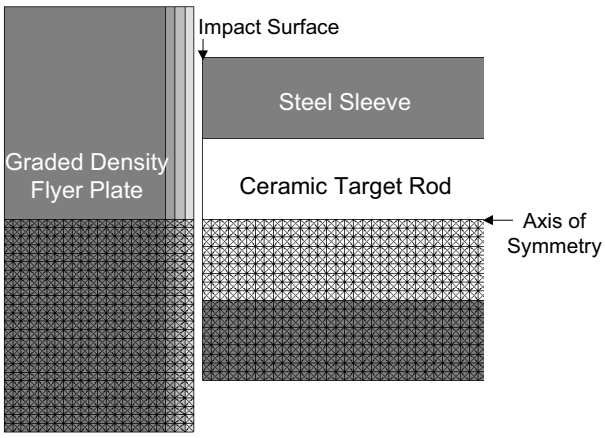

(b) Finite element grid (2D axisymmetric)

Figure 9 : Graded-density plate-on-rod impact

to simulate a "perfect" bond between adjacent layers of material. The ceramic target was modeled as a solid rod with a diameter of 1.9 cm and a length of about 7.4 cm, while the steel sleeve was modeled as a hollow rod with an inner diameter of 1.9 cm, an outer diameter of 3.8 cm, and the same length as the ceramic rod. Frictionless sliding was permitted between the inner surface of the sleeve and the outer surface of the ceramic rod. In the "regular" finite element grid (0.1 cm spacing), 1148 nodes and 2200 elements were used to describe the graded-density flyer plate, while 1340 nodes and 2520 elements were used to describe the ceramic rod, and 1340 nodes and 2520 elements were used to describe the steel sleeve. Though only one row of elements was defined for each of the thin (0.1-cm thick) graded-density layers (TPX, aluminum, and titanium), the overall "regular" grid resolution for the entire configuration was adequate. Figure

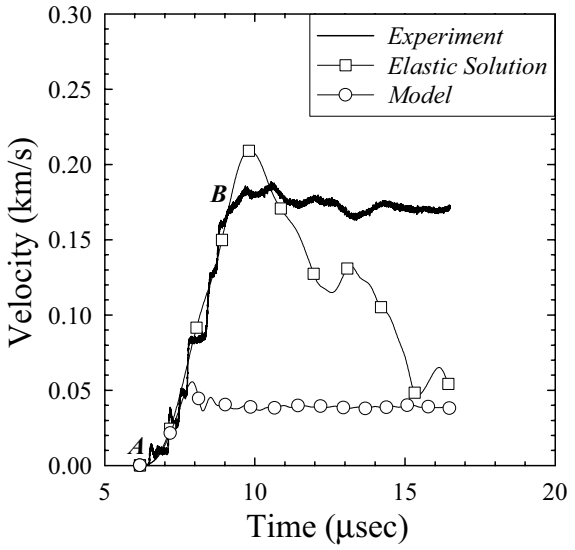

(a) Bare rod, impact velocity = 0.300 km/s

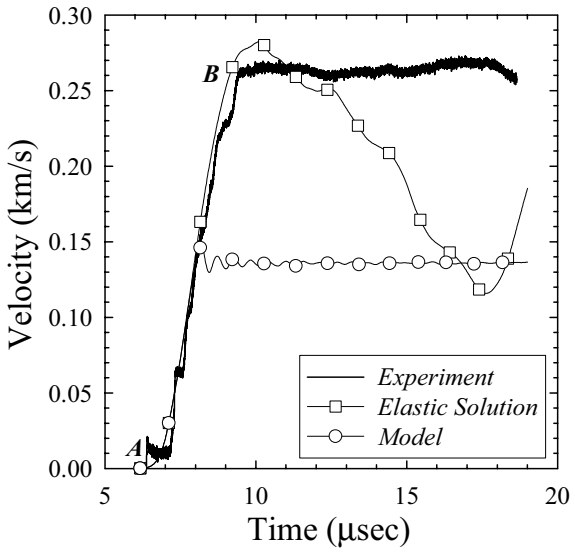

(b) Sleeved rod, impact velocity = 0.321 km/s

Figure 10 : Comparison of computed (elastic and a_o = 20 μm) velocity histories with data for graded-density plate impacting bare and sleeved AD995 ceramic rods

9(b) depicts a portion of the "regular" grid in the vicinity of the impact region. The "fine" (0.05 cm spacing) grid required 4495 nodes / 8800 elements for the graded-density flyer plate, 5753 nodes / 11172 elements for the ceramic rod, and 5753 nodes / 11172 elements for the steel sleeve.

We now present results from the simulations of the two experiments, with and without a steel sleeve, using the baseline model constants. Figures 10(a) and 10(b) compare the predicted axial velocities in the bare and sleeved rod tests, respectively. For comparison, we also included the elastic solutions with no crack damage. The elastic response results from the Lagrangian EPIC code matched very well with the Eulerian CTH code as presented by Chhabildas, Furnish, Reinhart, and Grady (1998). The average slopes of the computed velocity profiles (between points ***A*** and ***B*** in Fig. 10) agreed well with the data. However, the fine details of the ramping (staircasing) of the initial shock wave are absent in the modeling due to the relatively coarse mesh (0.1-cm size elements) used for the layers of TPX, aluminum, and titanium in the simulations. After reaching a peak velocity slightly higher than in the experiment, the rod rapidly decelerates in the elastic case. However, the experimentally measured velocity profiles indicate no deceleration of the rod, and the peak velocities remained relatively constant. The ceramic rod impacted by a single-density flyer plate also exhibited this constant-velocity behavior (shown in Section 3.3). We showed that the constant velocity was due to spalling of the ceramic rod near the free end.

The predicted peak velocity levels in both cases (with and without sleeve) were significantly lower than the measured values. As we mentioned earlier, this was due to the release waves from the damaged region (near the impact end) reaching the free end of the rod. There was no time for the initial shock wave to reach the experimental peak. Comparing the computed damage contour plots at 2 μs for the two cases, Fig. 11 reveals that the impact end of the bare rod has already fractured, while the sleeved rod is still intact and undamaged. The release waves from the damaged end propagate and overtake the initial shock wave and thus significantly reduce the velocity level at the free end. The delay in damage initiation in the sleeved rod prevents the unloading of the initial shock wave until a later time; this allows the velocity to increase to a higher value compared to that of the bare rod. Our detailed analysis of the simulation

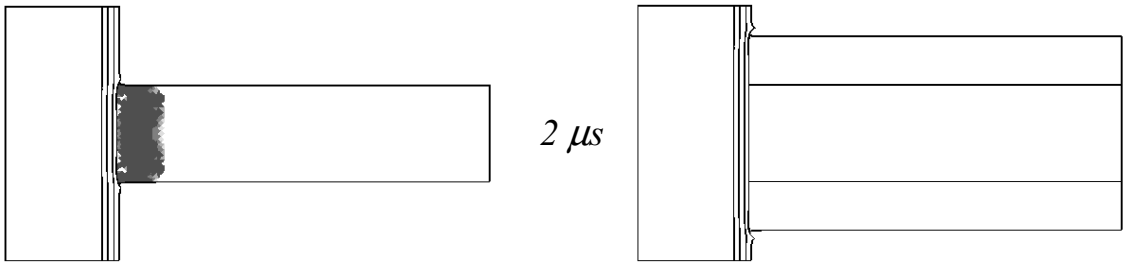

(a) Bare rod, impact velocity = 0.300 km/s (b) Sleeved rod, impact velocity = 0.321 km/s

Figure 11 : Effect of sleeve on model-predicted damage (shaded regions), from graded-density plate-on-rod impact simulations

results showed that the impact end of the rod remained under compression for a longer duration than the bare rod due to the confinement provided by the steel sleeve. The bare rod fractures due to tension created by the release waves from the edges of the impacted end of the rod. In the sleeved rod, the release waves do not emanate from the edges of the rod due to the steel sleeve. Since ceramics are significantly stronger in compression than tension, the fracture in the sleeved rod is postponed to a later time. The experimental data clearly showed that the peak velocities in the sleeved rods are higher than in the bare rods. The present ceramic constitutive model reproduced this trend very well; however, the calculated peak velocity levels were significantly lower than those measured experimentally. This was again due to the relatively large initial flaw size (20 μm) calibrated from the plate impact data (see Section 3.1).

We performed additional simulations using reduced values for the flaw size (a_o) and larger values for the dynamic friction coefficient (μ) to delay and limit the crack damage at the impact end. Figure 12 shows a reasonable match between the data and the model results for both the bare and sleeved rod cases, when a_o = 3 μm and μ = 0.90. In both cases, no significant damage occurs prior to the formation of a spall plane near the rod's free end. Consequently, the computed peak velocity levels are much higher, since there is no premature unloading of the initial shock wave.

For the sleeved-rod case, the "regular" and "fine" grids produced nearly identical velocity profiles. Both grids predicted the formation of a spall plane by 12 μs at about 2.3 cm from the rod's free end. However, for the bare-rod case, the "regular" grid produced a well- defined spall plane about 0.8 cm from the rod's free end (at 10.8 μs), while the "fine" grid produced a spall region about

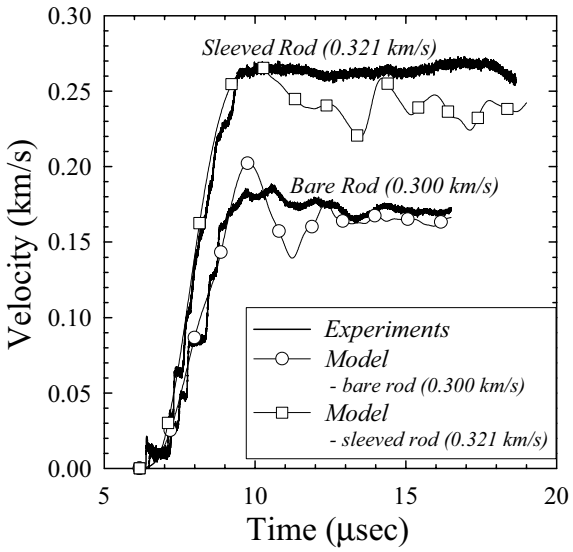

Figure 12 : Comparison of computed (a_o = 3 μm, μ = 0.90) velocity histories with data for graded-density plate impacting bare and sleeved AD995 ceramic rods

2 cm from the rod's free end (at 12 μs). Consequently, the bare-rod velocity histories exhibited grid-dependent behavior. The "fine"-grid solution's peak velocity was about 10% lower than that of the "regular" grid; after the initial peak, the "fine" grid's velocity profile remained below that of the "regular" grid (sometimes by as much as 30%), fluctuating between 0.120 and 0.165 km/s.

3.5 Projectile Penetration Simulations

Woolsey (1991) performed depth of penetration (DOP) experiments in which a tungsten long rod projectile is launched at a nominal velocity of 1.5 km/s onto a 15.24-cm-square ceramic tile that is laterally confined by a steel frame; the target assembly (tile and frame) is mechani-

cally clamped to a thick steel backup block. A schematic of this test configuration is shown in Fig. 13(a). The AD995 ceramic tiles that Woolsey tested were between 1.0 and 4.1 cm thick.

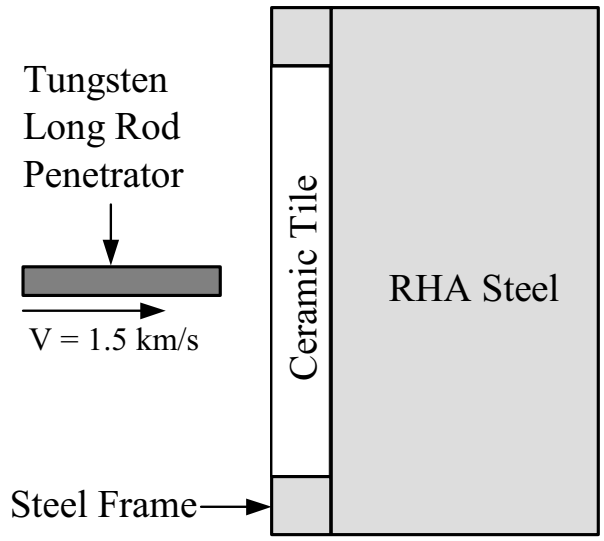

(a) Test configuration schematic

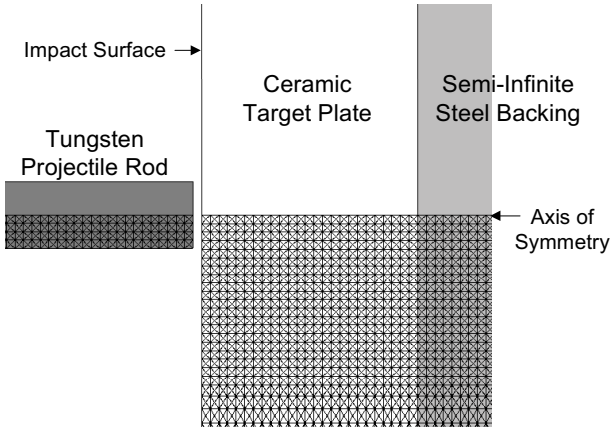

(b) Finite element grid (2D axisymmetric

Figure 13 : Depth-of-penetration (DOP) test

Since we used the 2D axisymmetric geometry option in EPIC to simulate the above DOP configuration, the target was assumed to be an AD995 ceramic disk (15.24 cm in diameter) backed by a thick steel cylinder (20.32 cm in diameter, 12.7 cm thick); the ceramic disk was also radially confined by a steel ring (2.54 cm wide, 5.08 cm thick) that was "clamped" to the steel cylinder. Since the lateral edges of the target are sufficiently far away from the impact region, the use of the 2D axisymmetric option does not significantly influence the computed DOP values for comparison with experiments. The projectile rod was 7.87 cm long and 0.787 cm in diameter.

In the "regular" finite element grid (0.1 cm spacing), 716 nodes and 1264 elements were used to describe the tungsten rod projectile, while 10168 nodes and 19904 elements were used to describe the steel holder. For the ceramic plates, the number of nodes ranged from 746 to 3586, while the number of elements ranged from 1400 to 7000, depending on the plate thickness (1.02 to 5.08 cm). To reduce the problem size, fixed nodal spacing in the radial direction (0.1 cm) was employed only inside the penetration zone (within 1.9 cm of the center of impact); the radial nodal spacing was increased geometrically beyond that point. The nodal spacing in the axial direction was constant through the entire thickness of the target. Figure 13(b) depicts a portion of the "regular" grid in the vicinity of the impact region. The "fine" (0.05 cm spacing) grid required 2729 nodes / 5120 elements for the tungsten rod, and 39627 nodes / 78400 elements for the steel holder; for the ceramic plates, the number of nodes ranged from 2891 to 14171, while the number of elements ranged from 5600 to 28000, depending on the plate thickness (1.02 to 5.08 cm).

We used the Johnson-Cook (JC) constitutive model (Johnson and Cook (1985)) to describe the strengths of the tungsten projectile and the steel frame/backup block. Elements on the contact surfaces were assumed to fail when their effective plastic strains reached 150%. For the tungsten material, we assumed density = 16.98 g/cm^3, melting temperature = 1723 $^\circ$K, and shear modulus = 124.1 GPa; for the tungsten EOS, we assumed Γ = 1.43, b_1 = 302.1 GPa, b_2 = 469.8 GPa, and b_3 = 334.9 GPa; and for the tungsten strength (JC model), we assumed A = 1.506 GPa, B = 0.1765 GPa, n = 0.12, C = 0.016, and m = 0. For the steel material, we assumed density = 7.823 g/cm^3, melting temperature = 1793 $^\circ$K, and shear modulus = 77.5 GPa; for the steel EOS, we assumed Γ = 1.16, b_1 = 163.9 GPa, b_2 = 294.4 GPa, and b_3 = 500.0 GPa; and for the steel strength (JC model), we assumed A = 0.7922 GPa, B = 0.5095 GPa, n = 0.26, C = 0.014, and m = 1.03.

Using the baseline ceramic model constants (see Section 2) to describe the response of the ceramic tile prior to pulverization, we arbitrarily assumed a "reasonable" value of 1.0 for β_p (the dynamic friction coefficient for granu-

lar motion), while $Y_p^{\max}$ (the pulverized strength cap) was assumed to be 4.5 GPa, as reported by Anderson, Johnson, and Holmquist (1995). The values of β_p and $Y_p^{\max}$ were not adjusted to match the data.

We simulated Woolsey's DOP test configuration for various AD995 ceramic tile thicknesses ranging from 1.02 to 5.08 cm. Figure 14 compares the measured and computed depths of penetration versus the areal density of the ceramic tiles. Since areal density is defined as mass per unit area, the areal density of a ceramic tile can be determined by multiplying its density by its thickness. The straight line in this figure is a linear least-squares fit to the experimental data. With a_o = 20 μm, the model consistently predicted too much residual penetration into the steel backup block. To investigate the effects of delaying the onset of damage in this configuration, the DOP experiments were re-simulated using smaller values for the initial crack size (a_o). As Fig. 14 indicates, the computed residual depths of penetration are very sensitive to a_o, especially for the thicker ceramic plates (higher areal densities). Overall, an initial microcrack size of 1.5 μm results in much better agreement with the experimental DOP measurements.

Figure 15 shows the final deformed finite element grid for the 2.54-cm thick ceramic plate (with a_o = 1.5 μm).

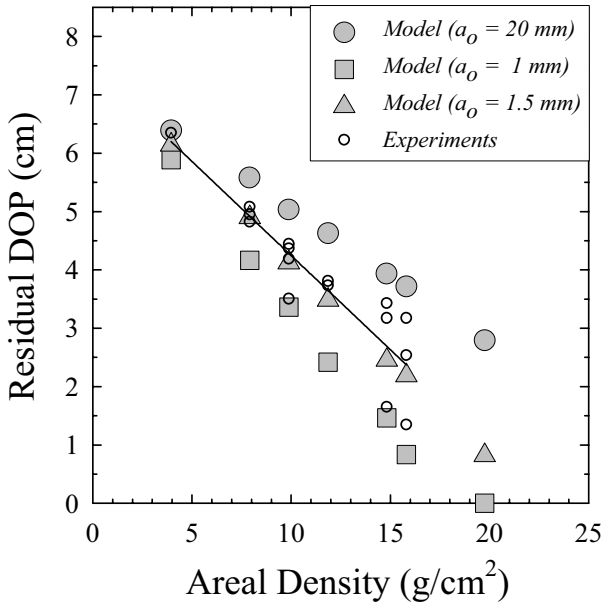

Figure 14 : Comparison of computed residual DOP with experimental data for AD995 ceramic

The eroded projectile is stopped at the bottom of the cavity in the target. For a_o = 1.5 μm, the computed cavity depths matched the experimental posttest measurements (see Fig. 14) for different thicknesses of ceramic plates. The cavity shown in this figure was created through EPIC's erosion algorithm, which removes highly strained (distorted) elements from the calculation based on a critical effective plastic strain criterion. When a finite element's aspect ratio (smallest height over largest width) becomes extremely small due to severe deformation (e.g., effective plastic strain of 150%) the solution

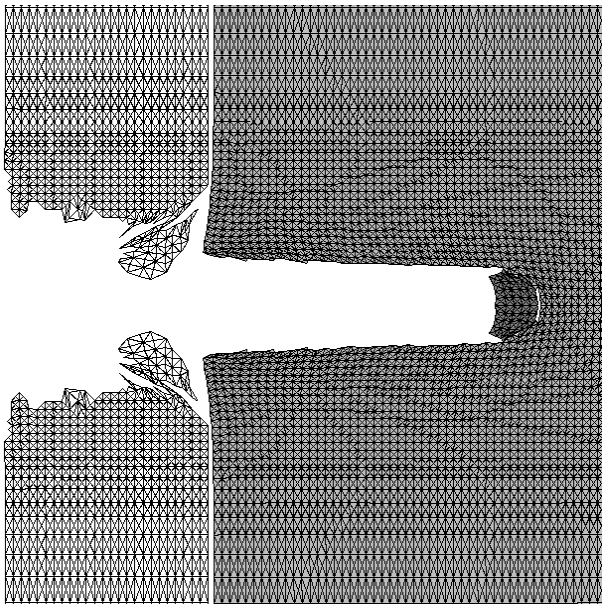

Figure 15 : Final deformed finite element grid for the 2.54-cm thick ceramic plate (with a_o = 1.5 μm)

time step size may drop to an unacceptable level. This is because the time step in an explicit shock-wave-based finite element code is determined from the characteristic time that a sound wave takes to travel through an element. To maintain a stable solution and to capture the shock wave effects, the time step must be a fraction of this characteristic time. Erosion of elements in both the projectile and target allows the EPIC code to model the penetration process. Incremental strain theories have been traditionally employed in most of the general purpose explicit finite element codes that are used in penetration application problems. Since these explicit codes use extremely small time steps, the strain rates are incrementally corrected for rotations at each time step; this provides a reasonable approach for modeling large deformations.

The ceramic model's DOP predictions were fairly insensitive to the finite element grid resolution. For each areal density (with a_o = 1.5 μm), the computed DOP's from the "regular" and "fine" grids were within 5% of each other, relative to the total penetration depth (ceramic tile thickness + residual DOP).

4 Summary

One of the most difficult tasks is to develop a well-defined computational methodology to determine accurate values for the constitutive model parameters. Ideally, direct experimental measurements of the material model constants would avoid any ambiguities. In reality, the model constants are, for the most part, extremely difficult to obtain directly from experiments; this is true for any ceramic model describing impact damage. For example, the present ceramic model's microcracking constants (a_o, N_o^*, μ, and n_1^-) are indirectly determined through a series of trial-and-error simulations until the computational results reasonably match the measured velocity/stress profiles.

At present, it is not possible to describe the shock and impact behavior of AD995 (or any other ceramic), using just one set of model parameters. We strongly believe that this is true for all the other ceramic models reported earlier in Section 1. Since the fracture initiation mechanisms vary widely with the applied loading conditions (stress/strain state, strain rate, and pressure), we need to model other damage mechanisms in addition to microcracking. For instance, under high triaxial tensile stresses, the pores and hard particles at triple-point grain junctions may instantaneously "burst" open to create isotropic spall failure as opposed to single-crack propagation.

Posttest examination of many of the targets (rods and plates) showed the presence of ring cracks, radial cracks, and fracture conoids. Accurate modeling of these macrocracks requires computationally intense algorithms such as contact, cohesive element, and adaptive mesh, as well as accurate nonlinear error estimates (Ortiz and Pandolfi (1999)). The use of SPH algorithms or meshless methods to describe ceramic fracture may eventually help us to model complex crack patterns (Atluri, Kim, and Cho (1999)). Recently, Abraham (2000) illustrated and validated a methodology (using a spanned length scale approach) to describe macrocrack propagation in a finite element simulation. Until these methods mature and become available in advanced general-purpose numerical codes, the use of conventional Lagrangian codes with some special features and reasonable constitutive models will continue to help impact design analyses involving ceramic materials.

This paper shows that using a microcrack-based scalar damage model in a conventional Lagrangian finite element code, numerical simulations can be performed to predict the overall response of ceramic materials subjected to a wide range of impact loading conditions. At present, it is very encouraging that the depths of penetration in ballistic tests can be predicted using a conventional Lagrangian code with a suitably calibrated constitutive description for the ceramic.

Acknowledgement: The authors would like to thank Dr. Douglas Templeton and Mr. Krishan Bishnoi of TARDEC, Warren, MI for their funding support of this work. This work was also supported in part by a grant of High Performance Computing (HPC) time from the DoD HPC Center at Aberdeen Proving Ground, MD.

References

Abraham, F. F. (2000): MAADLY Spanning the Length Scales in Dynamic Fracture, *CMES Computer Modeling in Engineering & Sciences*, Vol. 1, No. 4, pp.63-70.

Addessio, F. L.; Johnson, J. N. (1990): A Constitutive Model for the Dynamic Response of Brittle Materials. *J. Applied Physics*, Vol. 67, No. 7, pp. 3275-3286.

Anderson, C. E.; Johnson, G. R.; Holmquist, T. J. (1995): Ballistic Experiments and Computations of Confined 99.5% Al_2O_3 Ceramic Tiles. In M. Mayseless and S. R. Bodner (Eds): *Ballistics '95*, pp. 65-72. Israel.

Atluri, S. N.; Kim, H.-G.; Cho, J. Y. (1999): A critical assessment of the truly Meshless Local Petrov-Galerkin (MLPG), and Local Boundary Integral Equation (LBIE) methods. *Computational Mechanics*, Vol. 24, pp. 348-372.

Chen, Z.; Hu, W.; Chen, E. P. (2000): Simulation of Dynamic Failure Evolution in Brittle Solids without Using Nonlocal Terms in the Strain-Stress Space, *CMES:Computer Modeling in Engineering & Sciences*, Vol. 1, No. 4, pp.57-62.

Chhabildas, L. C.; Furnish, M. D.; Reinhart, W. D.; Grady, D. E. (1998): Impact of AD995 Alumina Rods. In Schimdt, S. C.; Dandekar, D. P.; Forbes, J. W. (Eds): *Shock Compression of Condensed Matter – 1997*, pp.

505-508. AIP Press.

Cook, W. H.; Rajendran, A. M.; Grove, D. J. (1992): An Efficient Numerical Implementation of the Bodner-Partom Model in the EPIC-2 Code. *Engg. Fracture Mechanics*, Vol. 41, No. 5, pp. 607-623.

Dandekar, D. P.; Bartkowski, P. (1994): Shock Response of AD995 Alumina. In Schmidt, S. C.; Shaner, J. W.; Samara, G. A.; Ross, M. (Eds): *High-Pressure Science and Technology - 1993, Part 2*, pp. 733-736. AIP Press.

Espinosa, H. D. (1995): On the Dynamic Shear Resistance of Ceramic Composites and its Dependence on Applied Multiaxial Deformation. *Int. J. Solids and Structures*, Vol. 32, No. 21, pp. 3105-3128.

Grady, D. E.; Moody, R. L. (1996): Shock Compression Profiles in Ceramics. Sandia Report, SAND96-0551, Sandia National Laboratory, Albuquerque, NM.

Grady, D. E.; Wise, J. L. (1993): Dynamic Properties of Ceramic Materials. Sandia Report, SAND93-0610, Sandia National Laboratory, Albuquerque, NM.

Gurson, A. L. (1977): Continuum Theory of Ductile Rupture by Void Nucleation and Growth; Part I: Yield Criterion and Flow Rules for Porous Ductile Materials. *J. Engr. Mat. Tech.*, Vol. 99, pp. 2-15.

Johnson, G. R.; Stryk, R. A.; Holmquist, T. J.; Beissel, S. R. (1997): Numerical algorithms in a Lagrangian hydrocode. Report No. WL-TR-1997-7039. Wright Laboratory, Eglin AFB, FL.

Johnson, G. R.; Holmquist, T. J. (1994): An improved computational constitutive model for brittle materials. In Schmidt, S. C.; Shaner, J. W.; Samara, G. A.; Ross, M. (Eds): *High-Pressure Science and Technology - 1993, Part 2*, pp. 981-984. AIP Press.

Johnson, G. R.; Cook, W. H. (1985): Fracture Characteristics of Three Metals Subjected to Various Strains, Strain Rates, Temperatures, and Pressures. *Engg. Fracture Mechanics*, Vol. 21, No. 1, pp. 31-48.

Kailasam, M.; Aravas, N.; Castañeda, P. P. (2000): Porous Metals with Developing Anisotropy: Constitutive Models, Computational Issues and Applications to Deformation Processing, *CMES: Computer Modeling in Engineering & Sciences*, Vol. 1, No. 2, pp. 105-118.

Kim, H. G.; Atluri, S. N. (2000): Arbitrary Placement of Secondary Nodes, and Error Control, in the Meshless Local Petrov-Galerkin (MLPG) Method, *CMES: Computer Modeling in Engineering & Sciences*, Vol. 1, No. 3, pp. 11-32.

Margolin, L. G. (1984): A Generalized Griffith Criterion for Crack Propagation. *Engineering Fracture Mechanics*, Vol. 19, No. 30, pp. 539-543.

Ortiz, M.; Pandolfi, A. (1999): A class of cohesive elements for the simulation of three-dimensional crack propagation. *Int. J. for Numerical Methods in Eng.*, Vol. 44, pp. 1267-1282.

Rajendran, A. M.; Kroupa, J. L. (1989): Impact Damage Model for Ceramic Materials. *J. of Appl. Phys.*, Vol. 8, No. 66, pp. 3560-3565.

Rajendran, A. M. (1994): Modeling the Impact Behavior of AD85 Ceramic Under Multiaxial Loading. *Int. J. Impact Engng.*, Vol. 15, No. 6, pp. 749-768.

Rajendran, A. M.; Grove, D. J. (1996): Modeling the Shock Response of Silicon Carbide, Boron Carbide, and Titanium Diboride. *Int. J. Impact Engng.*, Vol. 18, No. 6, pp. 611-631.

Simha, C. H. M. (1998): High Rate Loading of a High Purity Ceramic – One Dimensional Stress Experiments and Constitutive Modeling. Ph.D thesis, University of Texas, Austin, Texas.

Steinberg, D. J. (1991): Computer studies of the dynamic strength of ceramics. *J. de Physique IV*, Coll. C3 suppl., pp. 837-844.

Woolsey, P. (1991): Residual Penetration Ballistic Testing of Armor Ceramics. Unpublished Work, U. S. Army Materials Technology Laboratory, Watertown, MA.